

Broadband Digital Fourier Transform Spectrometer for On-Chip Wavelength Monitoring in the 2.3- μ m Wavelength Range

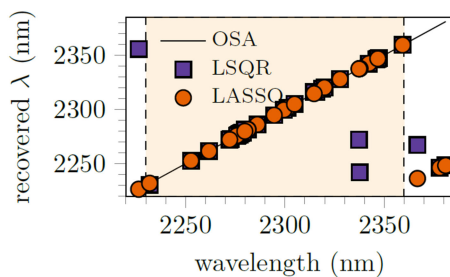
Volume 11, Number 3, June 2019

Fabio Pavanello, *Member, IEEE*

Anton Vasiliev

Muhammad Muneeb

Günther Roelkens, *Senior Member, IEEE*



DOI: 10.1109/JPHOT.2019.2914013

1943-0655 © 2019 IEEE

Broadband Digital Fourier Transform Spectrometer for On-Chip Wavelength Monitoring in the 2.3- μm Wavelength Range

Fabio Pavanello ^{1,2}, *Member, IEEE*, Anton Vasiliev ^{1,2},
Muhammad Muneeb,^{1,2}
and Günther Roelkens ^{1,2}, *Senior Member, IEEE*

¹Photonics Research Group, Ghent University—imec, 9052 Ghent, Belgium

²Center for Nano and Biophotonics, Ghent University, 9052 Ghent, Belgium

DOI:10.1109/JPHOT.2019.2914013

1943-0655 © 2019 IEEE. Translations and content mining are permitted for academic research only.

Personal use is also permitted, but republication/redistribution requires IEEE permission.

See http://www.ieee.org/publications_standards/publications/rights/index.html for more information.

Manuscript received January 22, 2019; revised March 27, 2019; accepted April 24, 2019. Date of publication April 29, 2019; date of current version May 10, 2019. The work of F. Pavanello was supported by the MIRPHAB Project (H2020-688265). The work of A. Vasiliev was supported by an FWO scholarship. (Fabio Pavanello and Anton Vasiliev contributed equally to this work.) Corresponding author: Fabio Pavanello (e-mail: fabio.pavanello86@gmail.com).

Abstract: We demonstrate a broadband digital Fourier Transform (dFT) spectrometer addressing wavelength monitoring applications in the 2.3- μm wavelength range. The spectrometer is built in a silicon-on-insulator platform and the design allows its fabrication with CMOS-compatible tools. We report an operating bandwidth of 130 nm around 2.3- μm wavelength using an efficient algorithm for sparse spectra to retrieve the wavelength with an accuracy of 100 pm. The spectrometer can also resolve two laser lines up for dFT spectrometers, which takes advantage of the sparse nature of the spectrum.

Index Terms: Silicon Nanophotonics, Integrated Photonic Systems, Spectroscopy.

1. Introduction

The wavelength range from 2 to 3 μm has been attracting considerable attention in recent years due to the growing interest in several applications of optical spectroscopy such as industrial and environmental monitoring, health care and chemical sensing [1]–[3]. The quest for integrated approaches to address these applications has fostered a large amount of work to develop platforms and components at wavelengths beyond the telecommunication window [3]–[5].

Arrayed-waveguide gratings (AWGs) and echelle concave gratings (ECGs) are well-known approaches in integrated photonics to build robust dispersive elements for spectrometers [6]–[8]. However, these approaches are characterized by a large footprint to accommodate a large bandwidth and high resolution. A different Fourier Transform (FT) based approach relies on integrated spatial heterodyne spectroscopy (SHS) [9]–[12]. For example, an SHS FT approach based on an array of Mach-Zehnder interferometers (MZIs) with linearly increasing optical path delays (OPDs) in a silicon-on-insulator (SOI) platform was recently demonstrated [11]. Although this approach does not suffer anymore from the resolution limitations of AWGs and ECGs, its footprint still scales linearly with the number of channels (to achieve a given resolution and spectral bandwidth simultaneously) as well as the number of output ports and required detectors, if no MZI modulation is

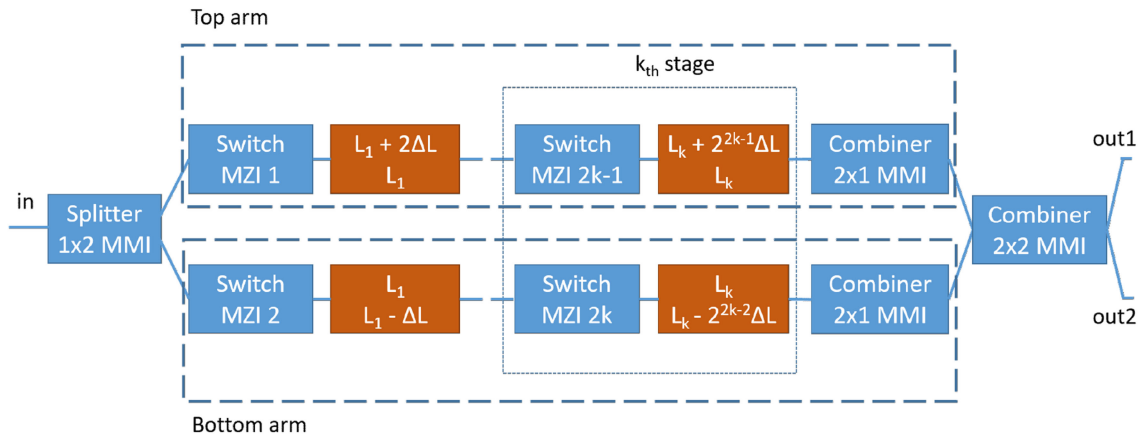


Fig. 1. Schematic of the dFT spectrometer design adopted in this work inspired by the initially dFT spectrometer proposed design [17]. Every stage has a top and a bottom arm with same lengths. $k = 1, 2, 3$ with $L_k = L_1 + 2^{2k-2}\Delta L$.

employed [8]. This latter limitation on the number of detectors is also present in other stationary FT approaches which require spatial or spectral sampling of a waveform [13]–[15]. Compressive sensing approaches can reduce the number of MZIs required to achieve a given resolution, however the scaling behavior remains still linear [11].

Recently, a new approach named digital Fourier Transform (dFT) spectrometer, schematically represented in Fig. 1, has been proposed to reduce the device footprint leading to an exponential scaling of the number of channels as a function of the number of elements providing an OPD, while using only a single detector [16]. The concept in Fig. 1 was originally implemented using a cascade of unbalanced MZIs where each of the stages comprises a switch. Depending on the specific configuration of each switch, OPDs between the top and the bottom arms of the dFT spectrometer can be modified in a reconfigurable manner. In fact, if the stages are switched purely in a binary way i.e. light is sent only in one of the two arms of each MZI stage, then 2^j configurations are possible where j represents the number of switches. This means that the number of channels scales exponentially with the number of stages according to [17]:

$$\delta\lambda \approx \frac{1}{2^N} \frac{\lambda^2}{n_g \Delta L} \quad (1)$$

where $\delta\lambda$ represents the channel width, N is the number of switches, n_g is the group index, λ is the wavelength in vacuum and ΔL is the increment step of the OPDs. Such configuration avoids to have 1 OPD element per channel as in the case of spatial heterodyne spectrometers, hence reducing the chip area required to implement all channels and their routing to photodetectors. It allows to build very compact spectrometers which can provide, with a limited number of stages and footprint, sub-nm spectral resolution according to the Rayleigh criterion [3], [18]. The dFT approach has been recently proposed and experimentally demonstrated near 1550 nm wavelength on an SOI platform over a bandwidth of 20 nm [16], [17]. For an arbitrary input spectrum, machine learning and regularization methods are required to ensure a reasonable spectral reconstruction. Another dFT spectrometer design has been recently proposed exploiting the same principles, but with a different way of implementing the OPD elements [19]. Here, we investigate the dFT spectrometer approach exploiting a variant of the design initially proposed by Kita and co-workers, but focusing on wavelength tracking applications [17]. Our design in the 2.3 μm wavelength range targets applications such as Vernier-based widely tunable lasers stabilization, which require wavelength monitoring as feedback mechanism [20]. Tunable and broadband integrated semiconductor lasers in this wavelength range are of great interest for various biomedical and gas sensing applications [21], [22]. Furthermore, this approach allows to monitor multiple closely (sub-nm) spaced laser

lines at the same time. Compared to prior art on dFT spectrometers, we provide further insight in terms of reconstruction techniques to achieve better accuracy, resolution and reduced number of configuration states. In particular, we demonstrate that the dFT approach for wavelength monitoring applications presents a large robustness which does not require to balance each MZI stage by means of tap ports as done by Kita and co-workers, while still achieving correct operation over a very broad wavelength range [17]. Several other approaches have been proposed so far for integrated wavelength monitoring, however they are generally characterized by a reduced bandwidth, large footprint, limited resolution or use of multiple photodetectors [20], [23]–[26]. Besides, they are limited to monitoring only a single line.

2. Theoretical Background and Design

The working principle of the dFT spectrometer approach (see Fig. 1) consists of acquiring the stationary interferogram for N different OPDs of the reconfigurable MZI from which the input can be reconstructed using FT-based methods [9]. Delay lines in the lower arm allow a negative (with respect to the common arm of length L_k in every stage) delay of $-2^{2k-2} \Delta L$, while those in the upper arm allow a positive (with respect to the common arm length L_k) delay of $2^{2k-1} \Delta L$, where ΔL is obtained from Eq. (1). Here, L_k is equal to $L_1 + 2^{2k-2} \Delta L$ with L_1 a constant offset. In practice, fabrication imperfections, dispersion, deviations in power splitting and loss effects complicate the direct FT reconstruction method. To circumvent this, a calibration step is performed which measures the exact wavelength response for each state of the re-configurable spectrometer. The $N \times M$ calibration matrix A represents the system response for $N = 2^j$ configurations of switches (all the binary combinations available) at M wavelength points. In this work j is 6 as we used 3 stages allowing $N = 64$ binary configurations. Once the calibration is performed i.e. the matrix A is obtained, several techniques can be adopted to retrieve the spectral response depending on the characteristics of the input signal. The spectroscopic system can be described by the following linear relation [16]:

$$y = Ax \quad (2)$$

where x is the unknown $1 \times M$ vector of wavelength points sampling the spectrum and y is the vector of the N measured configurations. Since $N < M$, this is an ill-posed linear problem and regularization methods are needed. In the current work only wavelength monitoring applications are targeted and therefore it is assumed that $x(\lambda)$ is a sparse vector. The unknown spectrum is computed using two methods: the first one involves the calculation of the Moore-Penrose least-squares (LSQR) inverse of A and the second one takes the sparsity into account by solving the convex optimization problem using the least absolute shrinkage and selection operator (LASSO) [11], [17]:

$$\min_{x_1, \dots, x_M \geq 0} \|Ax - y\|_2 \quad \text{subject to} \quad \|x\|_1 \leq \tau \quad (3)$$

with τ a pre-specified parameter which scales with the sparseness of the solution. For $\tau \rightarrow \infty$, the LSQR solution is found. The problem is solved efficiently using the non-negative spectral projected-gradient algorithm (SPGL) in Python [27], [28]. The design layout is reported in Fig. 2. A 400 nm thick silicon device layer and 3 μm thick buried oxide (BOX) layer have been used. A single-mode 800 nm wide rib waveguide, defined with a 180 nm deep etch, has been used for the MZIs and the routing, while the bending radius was 40 μm . The grating couplers are designed for 2.28 μm wavelength using a single partial etch step. The minimum optical path length difference ΔL was 10.825 μm and it was set by using Eq. (1) with a group index $n_g = 3.75$ and a spectral channel bandwidth $\delta\lambda = 2$ nm. The constant offset $L_1 = 770$ μm in each spiral corresponds to the minimum dimension allowing to have a spiral waveguide (for compactness) satisfying the design conditions i.e. bending radius and inter-spiral spacing. Grating couplers are used for input/output coupling. DC pads 150 $\mu\text{m} \times 100$ μm wide are used to drive the thermo-optic switches. The output is split into two arms to allow, at a later stage, the integration of a photodetector, while still being able to monitor optically the complementary output arm. Its overall footprint (complementary output excluded) is 4.57 mm \times 1.16 mm. The footprint can be further reduced by exploiting also a full etch step, reducing

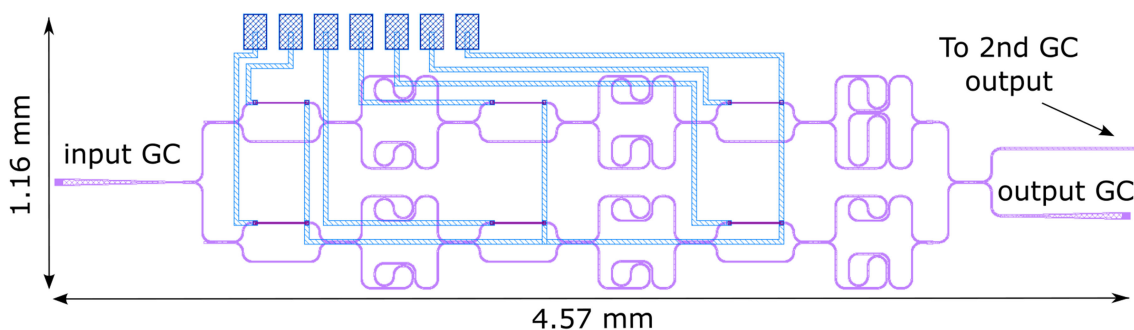


Fig. 2. Layout of the 3-stage dFT spectrometer. A complementary port, 1.45 mm away for the output grating, is not reported for drawing clarity.

the bending radius as well as by relaxing the constraint on matching the layout to the $500 \mu\text{m} \times 500 \mu\text{m}$ grid due to stitching issues proper of e-beam lithographic tools. We expect a factor of 3-4 improvement in the footprint by doing so. Heaters are placed on one arm and 2×2 MMIs are used at the input/output of the switches. A straight $2 \mu\text{m}$ wide waveguide with input/output grating couplers has been added to estimate the on-chip insertion loss.

3. Fabrication

For fast prototyping purposes, the patterning of the 400 nm thick device layer has been performed with e-beam lithography. However, all the minimum feature size dimensions can be achieved using industry-standard silicon fabrication tools. A 180 nm deep etching has been carried out using reactive ion etching to define rib waveguides. The layout has been matched to a $500 \times 500 \mu\text{m}^2$ grid in order to minimize stitching issues due to adjacent patterning fields. These issues would impact the insertion loss of the device and have been minimized by placing grid lines onto MMIs central multimode sections or onto $2 \mu\text{m}$ wide waveguides (with respective tapers) in other critical locations to increase the device tolerance and to reduce the insertion loss. Afterwards, a $1.5 \mu\text{m}$ thick SiO_2 layer has been deposited to enable heater integration. Heaters are based on a 150/10 nm thick Ti/Au bi-layer. Au wires and pads are then fabricated by UV lithography. The device is finally passivated with 700 nm thick BCB layer with openings on pads and grating couplers for probing.

4. Measurements and Analysis

The measurements have been performed using a Yokogawa AQ6375 optical spectrum analyzer and an IPG photonics SFTL-Cr-ZnS/Se laser. A polarization controller has been used to adjust for TE polarization at the grating coupler input. A 26 pin DC probe from GGB industries has been used to drive the heaters through an in-house designed 64 channel power supply.

The required P_π power for the heaters is estimated at 52 mW and was obtained from measuring an isolated 2×2 reference MZI with an extinction ratio larger than 30 dB. It is worth mentioning that the actual switching power for each stage is slightly different because of different heater resistances. However, such a difference does not impact the correct operation of the system as observed in our measurements. The on-chip insertion loss measured at the maximum transmission envelope for all the combinations was between 7 and 8 dB over a 130 nm wavelength span.

The calibration matrix A was collected on a wavelength grid spanning 160 nm with 0.5 nm steps, see also the normalized transmission in Fig. 3(a). An example of a spectrum for a given state is provided in Fig. 3(b). The collection was performed once at ambient room temperature over the course of few hours. The switching stages are not monitored (no weakly coupled port present) and the splitting power ratio varies among the switches decreasing the visibility of the interferometric

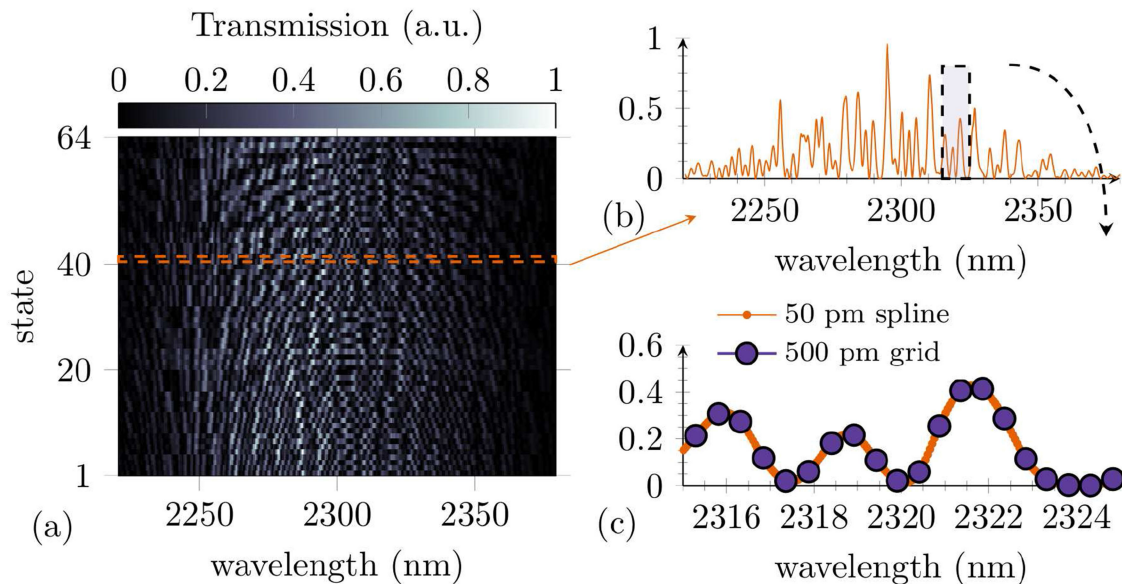


Fig. 3. Normalized calibration matrix for all 64 switch combinations (a) The broad wavelength dependency observed is due to the grating coupler response centered around $2.3 \mu\text{m}$. Such response is simply an additional contribution which remains constant for all the states. Hence this contribution does not impact the actual bandwidth of the device provided enough sensitivity of the detector. In a full system this contribution may not be present depending on the actual input/output light coupling to the chip. (b) The data is collected over the course of a few hours and without temperature control of the chip. An example for the switch state combination corresponding to $411 \mu\text{m}$ OPD is shown. (c) The calibration data is collected on a 500 pm wavelength step grid and interpolated using a spline function to a 50 pm regular grid.

fringes. Nonetheless, the linear system is proven to be remarkably robust against these issues. Differently from previous work on dFT spectrometers, here we show that, even if we do not observe a clear sinusoid for a given state (see Fig. 3(b)), the device performance for sparse spectra are not compromised [17].

It was found that the accuracy of the spectral recovery can be further increased from 500 pm to 100 pm by interpolating the calibration matrix data points onto a finer 50 pm grid using a spline function (see also Fig. 3(c)), while a linear interpolation does not improve accuracy, a smooth interpolation allows to improve the accuracy up to 100 pm . In what follows, a 64×3200 calibration matrix is therefore employed, spanning 160 nm with 50 pm wavelength grid spacing.

The signal-to-noise ratio (SNR) for such spectrometer used as wavelength monitor, defined here as peak amplitude with respect to the highest maximum at other wavelengths within the bandwidth, depends on the wavelength as well as on the reconstruction parameters and the wavelength window considered. In fact, by opportunely reducing such window, the SNR can be increased to arbitrary values. However, for wavelength monitoring applications, the SNR has a minor importance as only peak positions are required.

For wavelength tracking applications where the spectrum is sparse and the laser operation is in a single longitudinal mode, it is sufficient to record only the peak wavelength of the reconstructed spectrum. To this end, the LSQR solution, which is often adopted and included here for completeness, already provides a reasonable estimate. Two examples of spectral retrieval obtained from $N = 64$ consecutive optical power measurements are shown in Fig. 4. The LSQR solution has clearly more artifacts in the retrieved spectrum than LASSO, however the peak wavelength is close to the actual wavelength for both methods when limited to the operational bandwidth of 130 nm centered near $2.3 \mu\text{m}$. When the input spectrum is located near the edge of such bandwidth as in Fig. 4(b), aliasing is introduced leading to erroneous wavelength readings. The device bandwidth

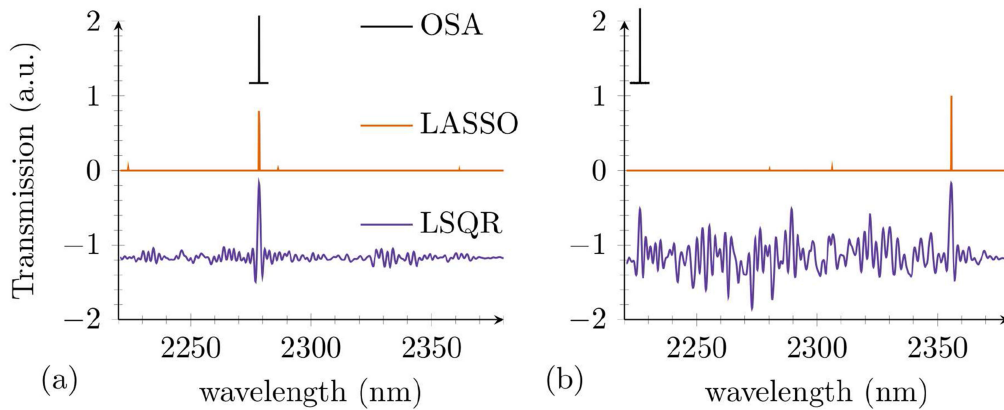


Fig. 4. Reconstructed spectra for an unknown laser input in the calibration span. The global maximum is used to assert the unknown laser wavelength. (a) Both LSQR and LASSO can recover the peak wavelength accurately. (b) Wavelengths at the edges of the operation bandwidth are reconstructed nearly 130 nm away in a consistent manner limiting the actual operation bandwidth. The normalized spectra are shifted vertically for clarity.

can be evaluated as [11]:

$$\Delta\lambda_{BW} = \frac{\lambda^2}{2n_g\Delta L} \quad (4)$$

which provides a value of 65 nm when evaluated at $\lambda = 2.3 \mu\text{m}$. However, due to the LASSO sparse algorithm and constraint conditions, only 1 peak is reconstructed (see Fig. 4(b)) at a distance from the actual wavelength matching twice the calculated $\Delta\lambda_{BW}$. For the LSQR algorithm, it is possible to distinguish 3 peaks in Fig. 4(b) located at the reference wavelength and at one and two $\Delta\lambda_{BW}$ away from it.

To estimate the accuracy of the device, 40 random wavelengths were selected for the laser input, spanning from 2220 nm to 2380 nm. A single interferogram was collected in each case and the calibration matrix was used to compute the LSQR and LASSO solutions. The global maximum of the normalized solution is then compared to the reading of the OSA, see Fig. 5(a). The parameter τ controls the maximum allowed L_1 -norm of the reconstructed spectrum and influences the spectral ripples of the reconstructed spectrum. It was found empirically that $\tau = 3.8$ was optimal to simultaneously track a single laser line and to resolve two lines for all conducted measurements. Alternatively, machine learning techniques could be used to search for the optimal parameter for each measurement separately without a priori knowledge of the examined spectrum at the cost of computational time [17]. The aliasing-free region for LASSO solutions is 130 nm and the wavelength accuracy of the method is about 100 pm. The zero-offset in Fig. 5(b) is due to the fact that the calibration was performed at different ambient temperature from the actual interferogram measurements. The temperature dependence of the spectrometer was measured to be 110 pm/°C by monitoring the device response shift with temperature using a temperature-controlled stage. The sources of uncertainty in our apparatus consist of temperature fluctuations of the controlled environment, which are estimated to account for ± 55 pm (± 0.5 °C), and of the OSA resolution, which was set to 50 pm. These values of uncertainty are consistent with the ± 100 pm retrieval accuracy reported.

It is believed that further improvement in accuracy can be readily achieved with active temperature stabilization of the chip and by fixing the optical input/output. The latter is obviously self-fulfilled for the case of a wavelength monitor for an integrated laser fabricated on the same chip. Besides, by using athermal MZIs configurations, the required power for active stabilization (if still necessary) can be further reduced.

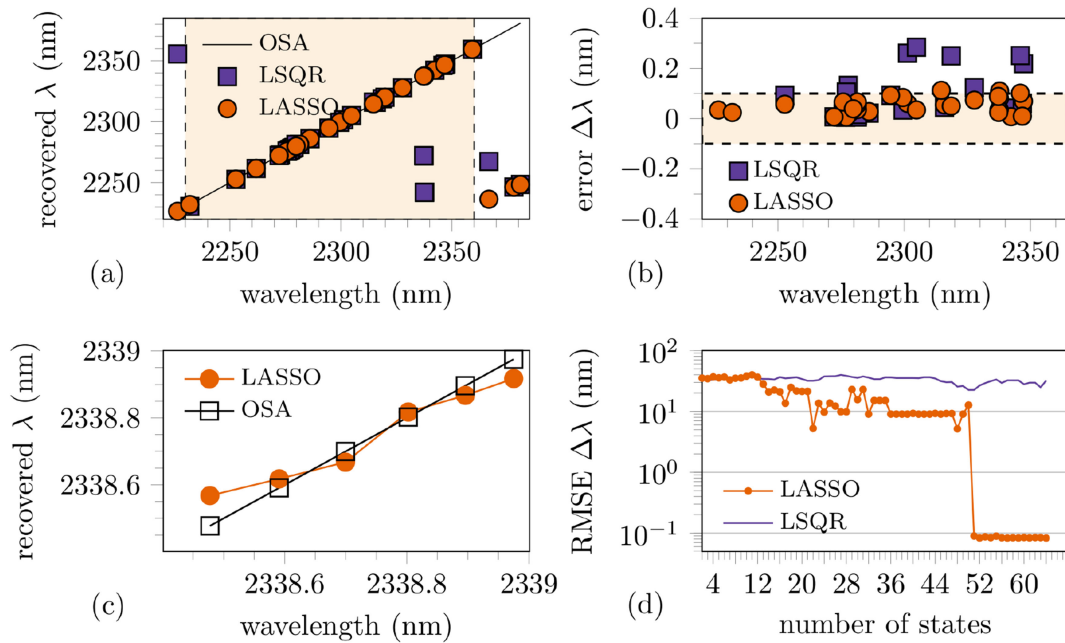


Fig. 5. Spectrometer performance in terms of tracking accuracy. (a) The wavelength is recovered without aliasing over a bandwidth of 130 nm. The uncertainty due to temperature fluctuations was estimated as ± 55 pm (0.5 °C difference), and the OSA resolution was set to 50 pm. (b) The LSQR algorithm produces outliers more frequently than LASSO. The accuracy is within 100 pm for 40 measurements within the bandwidth. The sparseness parameter is set to $\tau = 3.8$ for all measurements. The average error is not zero as the measurements were performed at a different ambient temperature with respect to the calibration. (c) Wavelength tracking of OPO laser module for a fine-tuning of the wavelength. The spectrometer can follow a 100 pm step sweep of the wavelength (calibration on a 500 pm grid). (d) The RMSE is calculated for all the measurements (40) within a 130 nm bandwidth. The compressive sensing (LASSO) algorithm makes it possible to reach optimal accuracy even when less than 64 states are used for the reconstruction, i.e. certain states are omitted randomly. The LSQR algorithm is less reliable due to a higher outlier count.

To assess the wavelength tracking of a fine wavelength sweep of a laser, the emission wavelength of an optical parametric oscillator (OPO) from Aculight was tuned piezo-electrically to successfully track the wavelength over a 600 pm window with the same 100 pm accuracy, see also Fig. 5(c). It is worth noting that without interpolation of the calibration matrix, the accuracy goes back to 500 pm (the measurement grid).

To estimate the resolution of the spectrometer, the Cr-ZnS/Se solid state laser was multiplexed with a custom GaSb-based external cavity laser from Brolis Semiconductors and tuned to a certain line separation, see Fig. 6. Clearly, the LASSO solution is superior to the LSQR solution for evaluating sparse multimode spectra. The spectrometer can resolve multiple laser lines with a separation down to 1.5 nm in a single iteration and down to 0.5 nm in a two step algorithm. In the first step, the reconstruction algorithm runs over the entire wavelength window (130 nm). Within this range, it locates the central wavelength, which is obtained as a weighted average over the power spectrum. In the second step, the reconstruction algorithm runs over a smaller wavelength window of 20 nm centered at the central wavelength determined in the first step. This novel approach of using a two-window reconstruction algorithm in dFT spectrometers allows to go in resolution beyond what was previously shown for such spectrometers using sparse spectra. In fact, compared to the channel resolution of 2 nm, a factor of 4 improvement is obtained in such a way. This improvement factor is twice higher than what reported in previous work for resolving 2 laser lines [17]. Such improvement comes from the sparse nature of the spectrum and from the LASSO algorithm utilized as pointed out in previous work in the two-fold improvement case [17].

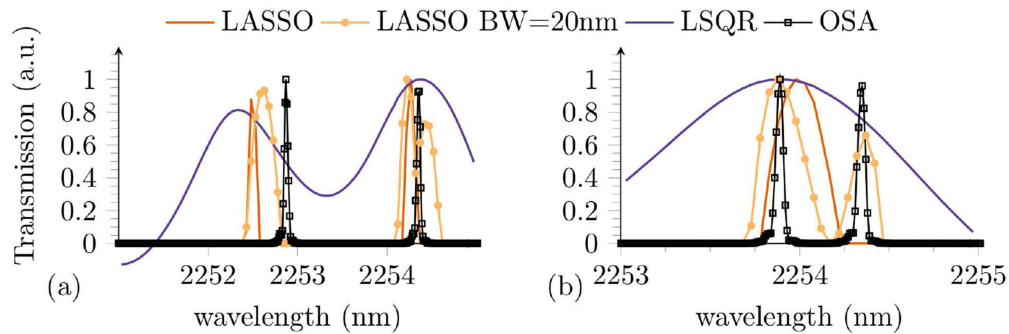


Fig. 6. The spectrometer can resolve multiple laser lines with a separation down to 1.5 nm in one iteration (a) and down to 0.5 nm in two steps (b). In the second step, the reconstruction algorithm is limited to a bandwidth window of 20 nm centered at the peak wavelength determined in the first step.

In the context of single mode wavelength monitoring, the presented dFT spectrometer can be made more efficient by leaving out a number of used OPD states. In this way, it is possible to reduce the required measurement time (dissipated power), computational resources and footprint without suffering any penalty on the accuracy. Due to the compressive sensing nature of LASSO, about 12 randomly selected states (12 rows, roughly 20% of all the states) can be omitted from the calibration matrix A , whilst retaining the same accuracy as shown in Fig. 5(d). This benefit is shown to apply also in the case of dFT spectrometers, similarly to other types of spectrometers [11]. The root-mean square error (RMSE) on the recovered wavelength is calculated for different total number of states (randomly selected) of the matrix A .

5. Conclusion

In conclusion, we have demonstrated a dFT spectrometer used as a wavelength monitor around $2.3 \mu\text{m}$ with a broad bandwidth of 130 nm. Although the spectrometer is fabricated with e-beam lithography, its design allows to use deep-UV lithography therefore supporting its CMOS-compatibility. The results demonstrate its potential to retrieve a given laser line with an accuracy of 100 pm. The low insertion loss and the large scalability showcase its potential as a wavelength monitor for broadband applications. Furthermore, we have demonstrated that balancing out the switching stages is not required to achieve correct operation and high performance over broad bandwidths thanks to the robustness of the dFT approach for wavelength monitoring applications. This approach can be extended to other platforms and wavelength ranges provided that they offer low propagation losses to allow high channel number scalability in terms of insertion loss. In fact, standard sub- μm thick SOI platforms would allow to extend this approach up to near $4 \mu\text{m}$ because of the limitation in Silicon dioxide absorption above $4 \mu\text{m}$. Other platforms based on Ge-rich SiGe can be used to extend the operation range up to $\approx 8 \mu\text{m}$ and potentially throughout the Ge transparency window up to $\approx 15 \mu\text{m}$ [29]. Compared to previous work on dFT spectrometers, we experimentally provided new insight in pathways to improve device performance and to reduce footprint and computational costs. Future work will be devoted to investigate other degrees of freedom available such as the possibility of using mix states instead of only a binary choice for the switches and to integrate it with state-of-the-art photodetectors.

References

- [1] R. Soref, "Mid-infrared photonics in silicon and germanium," *Nature Photon.*, vol. 4, no. 8, pp. 495–497, 2010. [Online]. Available: www.nature.com/naturephotonics
- [2] P. T. Lin *et al.*, "Label-free glucose sensing using chip-scale mid-infrared integrated photonics," *Adv. Opt. Mater.*, vol. 4, no. 11, pp. 1755–1759, Nov. 2016. [Online]. Available: <http://doi.wiley.com/10.1002/adom.201600440>

- [3] H. Lin *et al.*, "Mid-infrared integrated photonics on silicon: A perspective," *Nanophotonics*, vol. 7, no. 2, pp. 393–420, 2017. [Online]. Available: <https://doi.org/10.1515/nanoph-2017-0085>
- [4] T. Hu *et al.*, "Silicon photonic platforms for mid-infrared applications [Invited]," *Photon. Res.*, vol. 5, no. 5, pp. 417–430, 2017. [Online]. Available: <https://www.osapublishing.org/abstract.cfm?URI=prj-5-5-417>
- [5] A. Malik *et al.*, "Silicon-based photonic integrated circuits for the mid-infrared," *Procedia Eng.*, vol. 140, pp. 144–151, 2016. [Online]. Available: <http://linkinghub.elsevier.com/retrieve/pii/S1877705815043660>
- [6] A. Malik, M. Muneeb, Y. Shimura, J. Van Campenhout, R. Loo, and G. Roelkens, "Germanium-on-silicon planar concave grating wavelength (de)multiplexers in the mid-infrared," *Appl. Phys. Lett.*, vol. 103, no. 16, 2013, Art. no. 161119. [Online]. Available: <http://aip.scitation.org/toc/apl/103/16>
- [7] P. Barritault *et al.*, "Design, fabrication and characterization of an AWG at 4.5 μ m," *Opt. Exp.*, vol. 23, no. 20, pp. 26168–26181, Oct. 2015. [Online]. Available: <https://www.osapublishing.org/abstract.cfm?URI=oe-23-20-26168>
- [8] A. Vasiliev, M. Muneeb, J. Allaert, J. Van Campenhout, R. Baets, and G. Roelkens, "Integrated silicon-on-insulator spectrometer with single pixel readout for mid-infrared spectroscopy," *IEEE J. Sel. Topics Quantum Electron.*, vol. 24, no. 6, 2018, Art. no. 8300207.
- [9] M. Florjanczyk, P. Cheben, S. Janz, A. Scott, B. Solheim, and D.-X. Xu, "Multiaperture planar waveguide spectrometer formed by arrayed Mach-Zehnder interferometers," *Opt. Exp.*, vol. 15, no. 26, pp. 18176–18189, Dec. 2007. [Online]. Available: <https://www.osapublishing.org/oe/abstract.cfm?uri=oe-15-26-18176>
- [10] M. Nedeljkovic, A. V. Velasco, A. Z. Khokhar, A. Delage, P. Cheben, and G. Z. Mashanovich, "Mid-infrared silicon-on-insulator Fourier-transform spectrometer chip," *IEEE Photon. Technol. Lett.*, vol. 28, no. 4, pp. 528–531, Feb. 2016. [Online]. Available: <http://ieeexplore.ieee.org/document/7315027/>
- [11] H. Podmore *et al.*, "Demonstration of a compressive-sensing Fourier-transform on-chip spectrometer," *Opt. Lett.*, vol. 42, no. 7, pp. 1440–1443, 2017.
- [12] R. Uda, K. Yamaguchi, K. Takada, and K. Okamoto, "Fabrication of a silica-based complex Fourier-transform integrated-optic spatial heterodyne spectrometer incorporating 120 optical hybrid couplers," *Appl. Opt.*, vol. 57, no. 14, pp. 3781–3787, May 2018. [Online]. Available: <https://www.osapublishing.org/abstract.cfm?URI=ao-57-14-3781>
- [13] M. Madi, F. Ceysens, I. Shorubalko, H. P. Herzig, B. Guldemann, and P. Giaccari, "Lippmann waveguide spectrometer with enhanced throughput and bandwidth for space and commercial applications," *Opt. Exp.*, vol. 26, no. 3, pp. 2682–2707, 2018. [Online]. Available: <https://www.osapublishing.org/abstract.cfm?URI=oe-26-3-2682>
- [14] M. Yang, M. Li, and J.-J. He, "Static FT imaging spectrometer based on a modified waveguide MZI array," *Opt. Lett.*, vol. 42, no. 14, pp. 2675–2678, 2017. [Online]. Available: <https://www.osapublishing.org/abstract.cfm?URI=ol-42-14-2675>
- [15] Q. Liu *et al.*, "Integrated broadband dual-polarization Ge-rich SiGe mid-infrared Fourier-transform spectrometer," *Opt. Lett.*, vol. 43, no. 20, pp. 5021–5024, 2018. [Online]. Available: <https://www.osapublishing.org/abstract.cfm?URI=ol-43-20-5021>
- [16] D. M. Kita *et al.*, "On-chip infrared spectroscopic sensing: Redefining the benefits of scaling," *IEEE J. Sel. Topics Quantum Electron.*, vol. 23, no. 2, Mar./Apr. 2017, Art. no. 5900110.
- [17] D. M. Kita *et al.*, "High-performance and scalable on-chip digital Fourier transform spectroscopy," *Nature Commun.*, vol. 9, no. 4405, pp. 1–7, 2018. [Online]. Available: <http://dx.doi.org/10.1038/s41467-018-06773-2>
- [18] B. Smith, *Fundamentals of Fourier Transform Infrared Spectroscopy*. Boca Raton, FL, USA: CRC Press, Mar. 2011. [Online]. Available: <https://www.taylorfrancis.com/books/9781420069303>
- [19] R. A. Soref, F. D. Leonardis, V. M. N. Passaro, and Y. Fainman, "On-chip digital Fourier-transform spectrometer using a thermo-optical Michelson grating interferometer," *J. Lightw. Technol.*, vol. 36, no. 22, pp. 5160–5167, Nov. 2018.
- [20] M. Muneeb *et al.*, "Silicon-on-insulator shortwave infrared wavelength meter with integrated photodiodes for on-chip laser monitoring," *Opt. Exp.*, vol. 22, no. 22, pp. 27300–27308, 2014. [Online]. Available: <https://www.osapublishing.org/oe/abstract.cfm?uri=oe-22-22-27300>
- [21] R. Wang *et al.*, "Widely tunable 2.3 μ m III-V-on-silicon Vernier lasers for broadband spectroscopic sensing," *Photon. Res.*, vol. 6, no. 9, pp. 858–866, 2018. [Online]. Available: <https://www.osapublishing.org/abstract.cfm?URI=prj-6-9-858>
- [22] A. Vizbaras *et al.*, "Swept-wavelength lasers based on GaSb gain-chip technology for non-invasive biomedical sensing applications in the 1.7–2.5 μ m wavelength range," *Biomed. Opt. Exp.*, vol. 9, no. 10, pp. 4834–4849, Oct. 2018. [Online]. Available: <http://www.ncbi.nlm.nih.gov/pubmed/30319906>
- [23] W. H. Chung, H. Y. Tam, M. S. Demokan, P. K. Wai, and C. Lu, "Wavelength and power monitoring of DWDM systems using scanning F-P filter calibrated with a F-P laser," *Opt. Commun.*, vol. 210, no. 3–6, pp. 219–224, 2002. [Online]. Available: www.elsevier.com/locate/optcom
- [24] D. D'Agostino, *et al.*, "A monolithically integrated AWG based wavelength interrogator with 180 nm working range and pm resolution," in *Proc. Adv. Photon. Commun.*, Washington, DC, USA, Jul. 2014, Art. no. IM2A.4. [Online]. Available: <https://www.osapublishing.org/abstract.cfm?URI=IPRSN-2014-IM2A.4>
- [25] D. D'Agostino, R. Broeke, M. Boerkamp, J. Mink, H. Ambrosius, and M. Smit, "AWG based wavelength-meter with pm resolution," in *Proc. 17th Eur. Conf. Integr. Opt. Tech. Exhibition, 19th Microopt. Conf.*, 2014, vol. 2, pp. 3–4. [Online]. Available: www.tcpdf.org
- [26] C. Duchemin *et al.*, "Development of an integrated sub-picometric SWIFTS-based wavelength meter," *SPIE Proc., Photon. Instrum. Eng. IV*, vol. 10110, Feb. 2017, Art. no. 1011016.
- [27] E. Van Den Berg and M. Friedlander, "SPGL1: A solver for large-scale sparse reconstruction," 2015. [Online]. Available: <http://www.cs.ubc.ca/labs/scl/spgl1>
- [28] E. Van Den Berg and M. P. Friedlander, "Sparse optimization with least-squares constraints," *SIAM J. Optim.*, vol. 21, no. 4, pp. 1201–1229, Oct. 2011. [Online]. Available: <http://epubs.siam.org/doi/10.1137/100785028>
- [29] J. M. Ramirez *et al.*, "Graded SiGe waveguides with broadband low-loss propagation in the mid infrared," *Opt. Exp.*, vol. 26, no. 2, pp. 870–877, 2018. [Online]. Available: <https://www.osapublishing.org/abstract.cfm?URI=oe-26-2-870>